ACS OMEGA

http://pubs.acs.org/journal/acsodf

Article

Synergistic Effect of Redox Dual PdO_x/MnO_x Cocatalysts on the Enhanced H_2 Production Potential of a SnS/α-Fe_2O_3 Heterojunction via Ethanol Photoreforming

Hossein Etemadi, Tayyebeh Soltani, Hisao Yoshida, Yiming Zhang, Shane G. Telfer, Jenna K. Buchanan, and Paul G. Plieger*

Cite This: *ACS Omega* 2022, 7, 42347−42358

Read Online

ACCESS | Metrics & More | Article Recommendations | Supporting Information

ABSTRACT: In the quest for optimal H_2 evolution (HE) through ethanol photoreforming, a dual cocatalyst-modified heterocatalyst strategy is utilized. Tin(II) sulfide (SnS) was hybridized with α-Fe_2O_3 to form the heterocatalyst FeOSnS with a p−n heterojunction structure as confirmed by X-ray diffraction (XRD), Fourier transform infrared spectroscopy (FT-IR), UV−vis diffusive reflectance spectroscopy (UV−vis DRS), and Brunauer−Emmett−Teller (BET) techniques. PdO_x and PdO_x/MnO_x cocatalysts were loaded onto the FeOSnS heterocatalyst through the impregnation method, as verified by high-resolution transform electron microscopy (HRTEM), X-ray photoelectron spectroscopy (XPS), and elemental mapping. Photocatalytic ethanol photoreforming resulted in the production of H_2 as the main product with a selectivity of 99% and some trace amounts of CH_4. The FeOSnS2-PdO_x 2%/MnO_x 1% photocatalyst achieved the highest HE rate of 1654 μmol/g, attributed to the synergistic redox contribution of the PdO_x and MnO_x species.

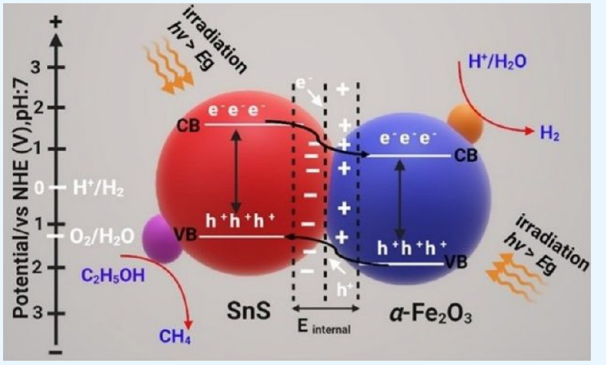

1. INTRODUCTION

Hydrogen (H_2) is a crucial requirement for many industrial chemical processes such as ammonia synthesis (∼50%), oil refining (∼40%), methanol synthesis (∼8%), and transportation. As of 2020, approximately 87 million tons of H_2 were generated worldwide, 95% of which is from fossil fuels by steam reforming of methane and other hydrocarbons as well as coal gasification. Nevertheless, the burning of fossil fuels releases large amounts of greenhouse gases such as CO_2 into the atmosphere, leading to global warming.[1,2] Solar energy is considered an ideal alternative to fossil fuels due to its high energy capacity (∼1.2×10^{14} kJ received at the Earth's surface every second), low cost, and abundance.[3] Solar-light-assisted splitting of H_2O over a TiO_2 photocatalyst was proposed in 1972 by Honda and Fujishima as a sustainable way for H_2 production.[4] Currently, the best performance has been achieved by TiO_2-based systems using UV light. The advantages of TiO_2 include availability, low cost, chemical stability, high chemical inertness, and nontoxicity.[5] Nevertheless, one disadvantage of TiO_2 is its limited activity in the visible spectrum due to its large band gap ($E_g \approx 3.2$ eV) and fast recombination of photogenerated electron−hole pairs.[6]

In spite of the significant body of research conducted with TiO_2, other UV-active photocatalysts such as ZnO[7] and $BiPO_4$[8] and even visible-active photocatalysts such as Bi_2WO_6,[9] WO_3,[10] and $BiVO_4$[11] with wide band gaps ($E_g < 3$ eV), the H_2 production efficiency achieved in water photosplitting is still too low for industrial viability. This is due to the occurrence of energetically favorable backward H_2 and O_2 reactions to yield water, fast recombination of photogenerated electron and hole (e^-/h^+) pairs due to the strong Coulombic force, limited light absorption efficiency, low charge transport properties, photocorrosion, and instability in water solutions.[12] An alternative strategy is the photoreforming of aqueous solutions containing biomass-derived oxygenates such as ethanol, glycerol, and glucose. Additionally, photoreforming can lead to the production of benzaldehyde, formaldehyde, and cyclohexanone as industrially attractive products.[13]

Hematite (α-Fe_2O_3) is an n-type photocatalyst and has been examined for photocatalytic H_2 production through H_2O splitting due to its abundance, nontoxicity, good corrosion resistance, low cost, and high photo-/thermostability.[14] Importantly, the narrow band gap of 1.9−2.2 eV renders it with the ability to absorb about 40% of the incident visible solar

Received: August 23, 2022
Accepted: October 7, 2022
Published: November 10, 2022

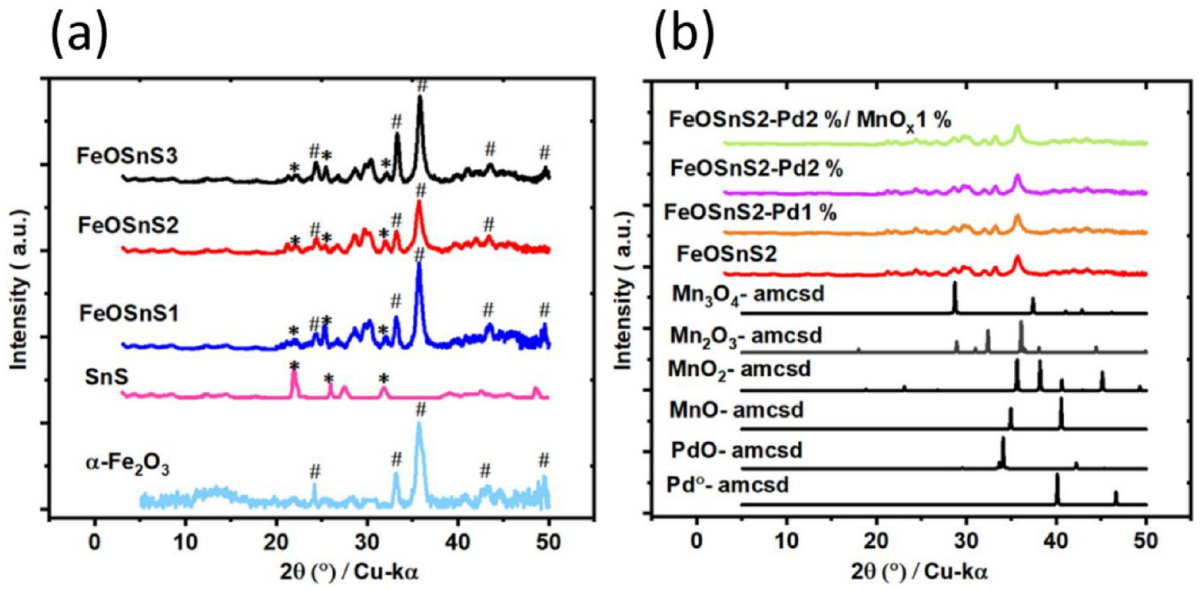

Figure 1. (a) PXRD patterns of α-Fe_2O_3 and SnS, FeOSnS1−3. (b) PXRD patterns of FeOSnS2-PdO_x/MnO_x catalysts.

energy.[15] Nevertheless, the performance of α-Fe_2O_3 is still limited by its low electrical conductivity (~10−14 Ω^{-1} cm^{-1}), short hole-diffusion distance (2−4 nm), poor electron−hole pair lifetime (<10 ps), poor oxygen evolution reaction (OER) kinetics, and weak charge mobility (10^{-2} to 10^{-1} cm^2 V^{-1} s^{-1}).[16,17] Furthermore, its conduction band (CB) is not negative enough to reduce H^+ ions to H_2.[18] Various strategies have been adopted to address these drawbacks associated with α-Fe_2O_3 for water splitting. These include the development of α-Fe_2O_3 nanoarchitectures with sizes smaller than its hole diffusion length,[19] surface state passivating,[20] the creation of oxygen vacancies,[21] doping of α-Fe_2O_3 with heteroatoms such as Sc, Ti, Cr, Mn, and Ni,[22] and construction of Z-scheme p−n junction heterostructures.[23] In contrast to water splitting, few studies have highlighted the H_2 production through ethanol photoreforming using α-Fe_2O_3. For example, Carraro et al. reported that control of the crystal phase of α-Fe_2O_3 can significantly improve the H_2 production potential. The results revealed H_2 production rates of 40, 225, and 125 mmol h^{-1} m^{-2} for α-Fe_2O_3, β-Fe_2O_3, and ε-Fe_2O_3, respectively, through photoreforming of ethanol/water solutions under irradiation from a 150 W Xe lamp.[24] Wender et al. reported an improved H_2 production rate of 546 mmol h^{-1} g^{-1} for an α-Fe_2O_3 nanoring loaded with a 7% $Co(OH)_2$ cocatalyst versus 350 μmol h^{-1} g^{-1} for pure α-Fe_2O_3.[25]

Tin monosulfide (SnS) is a p-type semiconductor with excellent optoelectric characteristics.[26] SnS has an indirect band gap of 1−1.2 eV, a direct optical band gap of 1.2−1.5 eV, high absorption coefficient (10^4−10^5 cm^{-1} in the visible region), high conductivity, low cost, and high charge mobility.[27] Cocatalysts such as noble metals (Ni, Pt, Au, Pd, and Rh and Ag) or transition metal oxides (NiO, Co_3O_4, MnO_x, and CuO_x) have been extensively examined as important charge mediators to boost photocatalytic performance.[28]

In this contribution, we have optimized the conduction band energy of α-Fe_2O_3 through hybridization with SnS to improve the reduction of H^+ ions to H_2 via ethanol photoreforming. Additionally, the FeOSnS heterocatalyst was decorated with PdO_x and MnO_x dual cocatalysts to boost the H_2 production efficiency. This is the first report on the tertiary mixture of α-Fe_2O_3/SnS with dual redox cocatalysts for photocatalytic H_2 production.

2. RESULTS AND DISCUSSION

2.1. Synthesis of the Heterocatalysts and Cocatalysts. FeOSnS heterocatalysts were prepared using the *in situ* chemical precipitation method with SnS:α-Fe_2O_3 ratios of 1:1 w/w (FeOSnS1), 1.5:0.5 w/w (FeOSnS2), and 0.5:1.5 w/w (FeOSnS3). An impregnation method was then used to load PdO_x and MnO_x catalysts onto the FeOSnS2 catalyst, forming FeOSnS2-PdO_x 1%, FeOSnS2-PdO_x 2%, and FeOSnS2-PdO_x 2%/MnO_x 1% catalysts based on the mass percentages of the loaded cocatalysts. The synthesized catalysts were characterized by X-ray diffraction, transmission electron microscopy (TEM), scanning electron microscopy (SEM), X-ray photoelectron spectroscopy (XPS), atomic absorption spectroscopy (AAS), and UV−vis diffuse reflectance spectroscopy (UV−vis DRS).

2.2. X-ray Diffraction. The crystalline phase and purity of the as-prepared α-Fe_2O_3, SnS, FeOSnS1−3, and FeOSnS2-PdO_x/MnO_x catalysts were studied by powder X-ray diffraction (PXRD) (Figure 1). Pristine α-Fe_2O_3, which was synthesized from the decomposition of $Fe(acac)_3$ in DMF in the presence of PVP surfactant at 180 °C, presents distinct diffraction peaks at 2θ = 24.1°, 33.1° (main characteristic peak), 35.6°, 40.8°, and 49.4°, assigned to the crystal planes of (012), (104), (110), (113), and (024), respectively (Figure 1(a)).[29] For pristine SnS, formed from $SnCl_2$ and sulfur in the presence of PVP in DMF, the characteristic diffraction peaks were observed at 2θ = 21.9°, 25.9°, 27.6°, 31.9°, 39.2°, 42.6°, 45.5°, and 48.5° corresponding to the (011), (012), (102), (004), (113), (021), (015), and (023) diffraction planes, respectively (Figure 1(a)).[30]

In the PXRD pattern of FeOSnS1−3 heterocatalysts (Figure 1(a)), a series of characteristic diffractions peaks from α-Fe_2O_3 (indicated by the symbol #) and SnS (indicated by the symbol *) are observed. In addition, the main diffraction peaks in the heterocatalysts have minor changes compared with pristine α-Fe_2O_3 and SnS, suggesting that the hybridization had a negligible influence on the original crystal structure of the constituents. This also indicates that any improvement in the photocatalytic potential is not caused by alteration of the crystal

https://doi.org/10.1021/acsomega.2c05410
ACS Omega 2022, 7, 42347−42358

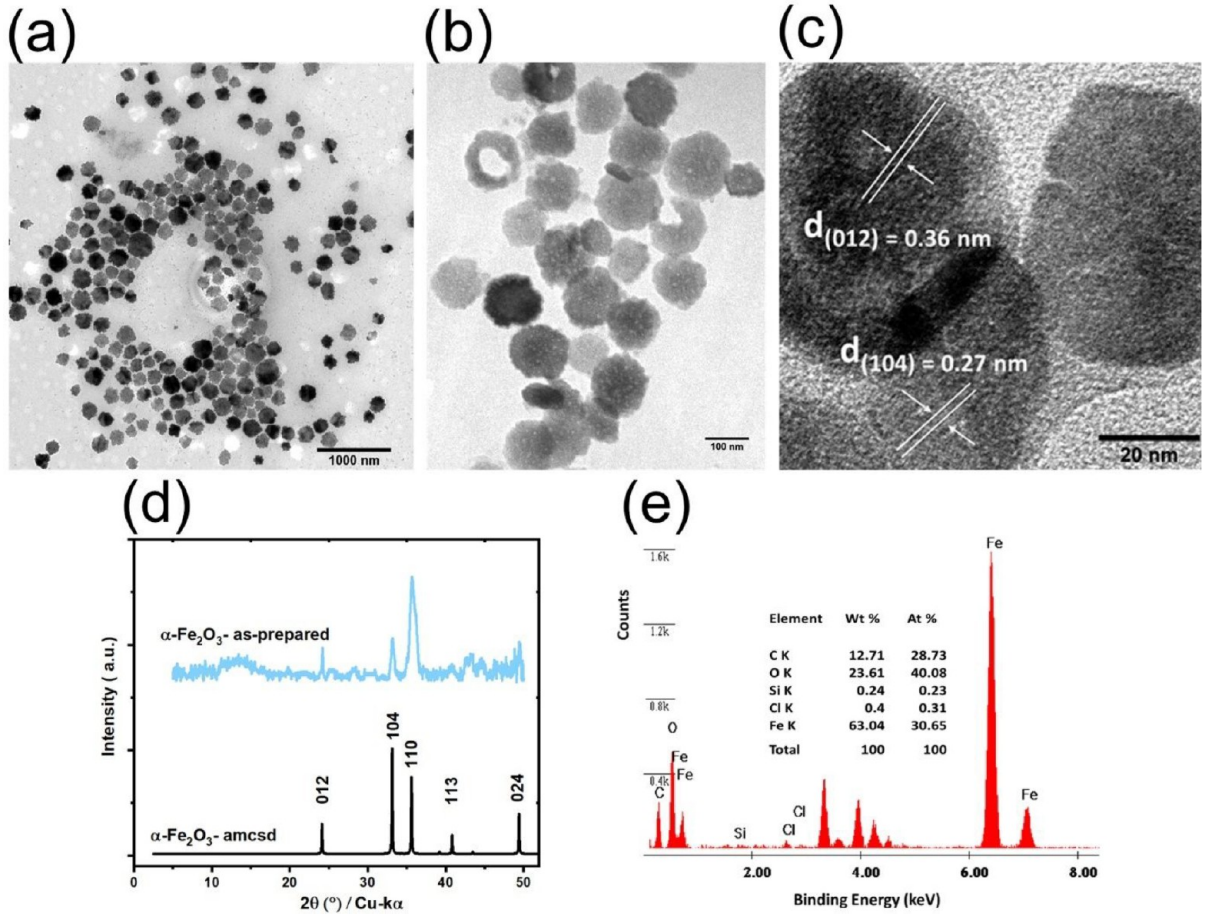

Figure 2. (a)−(c) TEM and HRTEM image, (d) PXRD pattern (pattern for α-Fe_2O_3 (AMCSD card no. 0000143) is shown for comparison), and (e) EDS spectra of the α-Fe_2O_3 catalyst.

structure of the constituents.[31] It is worth noting that we used an *in situ* chemical precipitation method to synthesize FeOSnS heterocatalysts rather than direct physical mixing. The reason was to improve the charge transfer between the two photocatalysts through the strong chemical bonding formed at the interface.[32] In the case of the FeOSnS2-PdO_x/MnO_x catalyst, no obvious characteristic peaks of PdO_x species (metallic Pd or PdO) or MnO_x species (MnO, Mn_2O, Mn_2O_3, and Mn_3O_4) were detected (Figure 1(b)). This was due to the low loading amount (1 and 2%) of the PdO_x and MnO_x cocatalysts and the high dispersion of catalyst on the heterostructure, in accordance with other results in the literature.[33−35]

2.3. Transmission Electron Microscopy. Transmission electron microscopy images of synthesized α-Fe_2O_3 display nanometer sized particles with high monodispersity and an average diameter of 120 ± 24 nm (Figure 2(a) and 2(b)). The high-resolution TEM (HRTEM) image reveals lattice spacing of 0.36 and 0.27 nm, referring to (012) and (104) crystal planes, respectively (Figure 2(c)).[36] The observed values match with the PXRD pattern of the standard American Mineralogist Crystal Structure Database (AMCSD card no. 0000143) for rhombohedral (hexagonal) α-Fe_2O_3 with lattice constants of a = b = 0.503 nm and c = 1.377 nm (Figure 2(d)). The characteristic peaks for iron (Fe), oxygen (O), and carbon (C) were detected in the EDS spectrum of α-Fe_2O_3 (Figure 2(e)).[37] We have attributed the trace amounts of chloride to the KCl used for the shape-controlled synthesis.

The TEM image of SnS reveals the characteristic formation of interconnected flower-like structures (Figure 3(a)).[38] Each nanoflower consists of thin 2D nanosheets with sharp edges growing anisotropically in all directions (Figure 3(b)).[39] The HRTEM image reveals lattice spacing of 0.34 nm ascribed to the (012) crystal plane (Figure 3(c)).[40] The observed values match with the PXRD pattern of the standard American Mineralogist Crystal Structure Database assigned to the orthorhombic phase of SnS with lattice parameters a = 0.433, b = 1.11, and c = 0.398 nm (AMCSD card no. 0018115) (Figure 3(d)). The EDS spectra of SnS exhibit the signals for C, Sn, and S atoms (Figure 3(e)). The presented data reveal an Sn/S atomic ratio of 70.3, indicating the synthesized SnS catalyst deviated from stoichiometry. This high sulfur deficiency is due to postcalcination of SnS which results in significant evaporation of sulfur due to its high volatility.[41] Banu et al. reported the atomic ratio of Sn/S = 21.97 after annealing the prepared SnS thin films at 500 °C for 30 min.[42]

The TEM image of the α-Fe_2O_3 and SnS heterostructure (FeOSnS) shows that α-Fe_2O_3 is dispersed onto the surface of SnS nanoflowers with close contact between the two components (Figure 4(a)). This is favored for forming a heterostructural interface through interactions between the two photocatalysts, which can promote effective charge separation.[43,44] Furthermore, α-Fe_2O_3 and SnS are shown in the TEM images to retain their original shape without morphological changes after hybridization.[45] The TEM image of FeOSnS2-PdO_x 2% shows the morphology changes after loading PdO_x

https://doi.org/10.1021/acsomega.2c05410
ACS Omega 2022, 7, 42347−42358

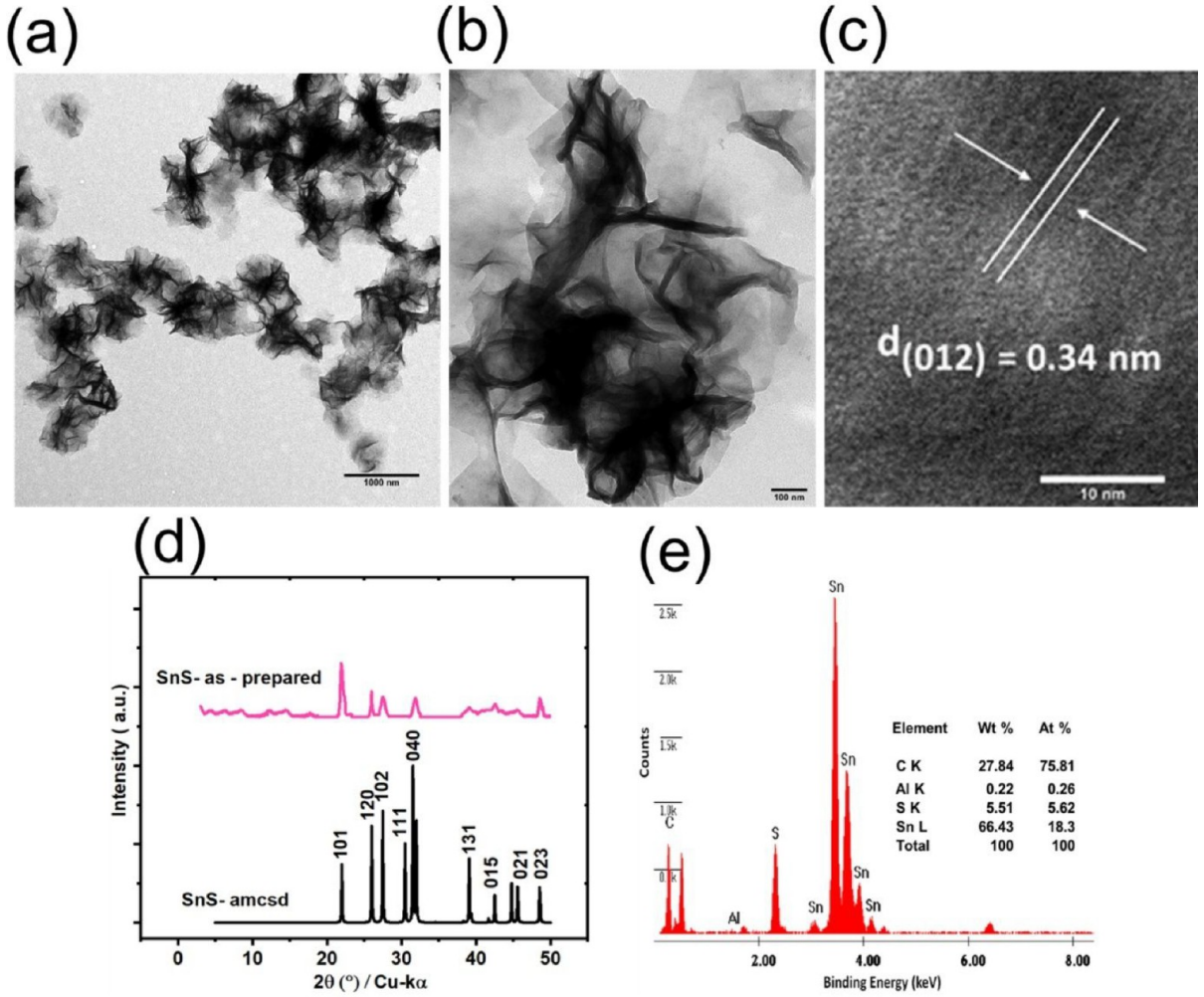

Figure 3. (a)−(c) TEM and HRTEM images, (d) PXRD pattern (a pattern for SnS (AMCSD 0018115) is shown for comparison), and (e) EDS spectra of the SnS catalyst.

nanoparticles, in which the PdO_x nanoparticles are observed as black dots, dispersed on the surface of the heterocatalyst (Figure 4(b)). The size distribution profile shows an average size of 3.7 ± 1 nm (Figure S1). The TEM image of FeOSnS2-PdO_x 2%/MnO_x 1% exhibits the same morphology as FeOSnS2-PdO_x 2% with PdO_x nanoparticles seen as black dots, with an average size of 2.8 ± 0.87 nm (Figures 4(c) and S1). Notably, the MnO_x cocatalyst is not localized due to the low concentration. Scanning TEM (STEM) imaging using a High-Angle Annular Dark Field (HAADF) detector and an Energy-Dispersive Spectroscopy (EDS) elemental mapping evidenced the presence of C, O, Fe, Sn, S, and Pd elements without any signal for Mn in the FeOSnS2-PdO_x 2%/MnO_x 1% catalyst (Figure 4(d)).

2.4. Heterostructure Formation. The heterostructure formation was further studied using the Brunauer−Emmett−Teller (BET) method. We calculated the specific surface area (S_{BET}) and pore volume of the synthesized catalysts from adsorption−desorption isotherms. SnS presented S_{BET} and pore volume values of 60.9 $m^2\ g^{-1}$ and 0.063 cc/g which were higher than that of α-Fe_2O_3 with S_{BET} and pore volume values of 24.6 $m^2\ g^{-1}$ and 0.031 cc/g, respectively (Figure 5(a)). The higher surface area of the SnS catalyst is due to its hierarchical porous architecture, whereas in the case of α-Fe_2O_3, a small surface area and low pore volume indicate that the α-Fe_2O_3 primary crystals are densely packed as evidenced by TEM results.[46] Integration of α-Fe_2O_3 with SnS resulted in FeOSnS heterocatalysts (FeOSnS1−3) with reduced specific surface areas and pore volumes (Figure 5(a) and Table S1). This is due to the decrease in the pore volume of SnS or the blocking of the porous channels of SnS when coupling with α-Fe_2O_3, as reported by Yousatit et al.[47] The pore volume and diameter values for FeOSnS1−3 catalysts were not consistent with the initial ratios (Table S1), indicating that α-Fe_2O_3 nanoparticles are not uniformly distributed on SnS which agrees with the TEM results. Furthermore, loading of the cocatalyst reduced the surface area and pore volume of the FeOSnS2 heterocatalyst from 24.9 m^2/g and 0.008 cc/g down to 15.6 m^2/g and 0.005 cc/g for FeOSnS2-PdO_x 2%/MnO_x 1% (Figure 5(b) and Table S1). This phenomenon is attributed to the partial surface coverage of the heterocatalyst by the deposited cocatalysts.[48]

The heterostructure formation was further confirmed by attenuated total reflection-Fourier transform infrared (ATR-FTIR) and UV−vis diffuse reflectance spectroscopy (UV−vis DRS) results (see Figures S2 and S3 in the Supporting Information). XRD and FT-IR studies could not confirm the presence of the cocatalysts in the FeOSnS heterostructures, but EDS analysis was able to. Unfortunately, as the detection limit of EDS used in this study was <1 wt %, the technique was not able to give accurate quantitative values (see Figure S4 in the Supporting Information). Atomic absorption spectroscopy

https://doi.org/10.1021/acsomega.2c05410
ACS Omega 2022, 7, 42347−42358

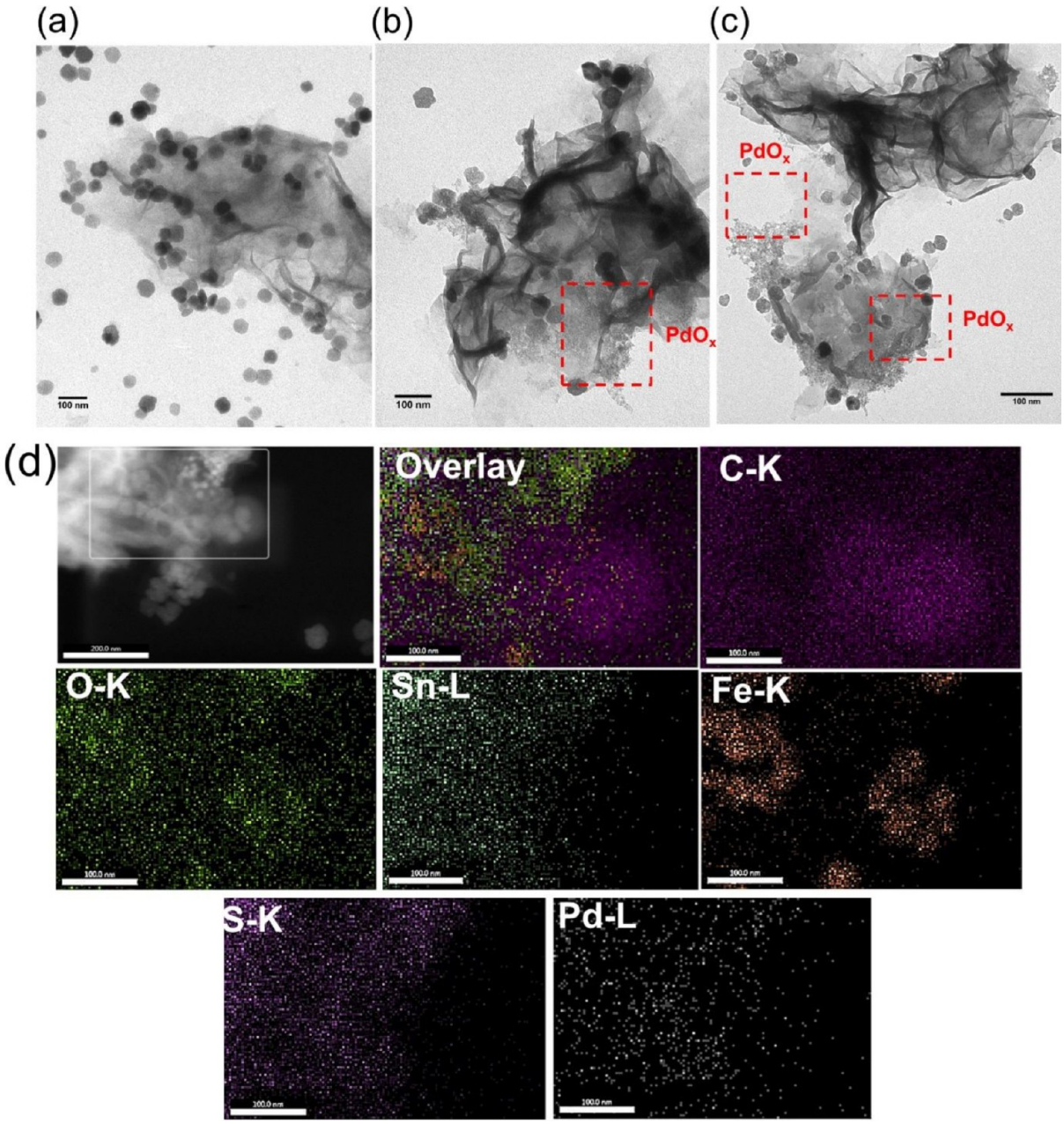

Figure 4. (a)−(c) TEM images of FeOSnS2, FeOSnS2-PdO$_x$ 2%, and FeOSnS2-PdO$_x$ 2%/MnO$_x$ 1% catalysts. (d) HAADF-STEM and EDX elemental mapping images of FeOSnS2-PdO$_x$ 2%/MnO$_x$ 1% catalyst.

(AAS) was therefore utilized to confirm the content of the cocatalyst in the synthesized FeOSnS2 heterocatalyst (see Table S2 in the Supporting Information).

2.5. X-ray Photoelectron Spectroscopy. To further explore the presence of the cocatalysts and identify the related oxidation states, XPS was performed. Wide-scan survey spectra revealed photoelectron lines at binding energies (BEs) of 23.6 eV (Sn 4d), 153−175 eV (S 2p), 278−300 eV (C 1s), 328−348 eV (Pd 3d), 480−505 eV (Sn 3d), 520−545 eV (O 1s), 556−630 eV (Mn 2p), and 697−745 eV (Fe 2p), at the surface (≤3 nm), as illustrated in Figure 6a. This is consistent with the EDS results and revealed the successful impregnation of PdO$_x$ and MnO$_x$ cocatalysts on FeOSnS2. The high-resolution XPS window of the C 1s core level (Figure 6(b)) is deconvoluted into three peaks at BEs of 284.8, 285.7, and 288.3 eV, respectively, corresponding to C−C sp^2 from PVP molecules and adventitious carbon, a C−OH bond, and a carbonyl (−OC═O) bond, respectively.[49] The O 1s core-level spectra (Figure 6(c)) exhibit a high intensity peak at ∼530.3 eV corresponding to the lattice oxygen of iron−oxygen bonds (Fe−O) of the α-Fe$_2$O$_3$ component in the heterocatalyst. The high intensity of the peak is due to the high number of iron ions (Fe^{3+}) strongly interacting with the lattice oxygen (O^{2-}) in the crystal lattice. The peak centered at 532.2 eV is associated with the surface −OH groups (adsorbed water) and oxygen bonded with the PVP C atoms (Fe−O−C bond).[50] As can be seen in the wide-scan survey spectra and high-resolution S 2p photoelectron spectra (Figure 6(d)), the peaks at 161−162 and 162−163 eV corresponding to S 2p$_{3/2}$ and S 2p$_{1/2}$ are absent. This is due to sulfur being present in amounts lower than the detection limit for XPS,[51] which is in accordance with EDS and elemental mapping results.[52,53] Sn manifests itself with strong peaks

https://doi.org/10.1021/acsomega.2c05410
ACS Omega 2022, 7, 42347−42358

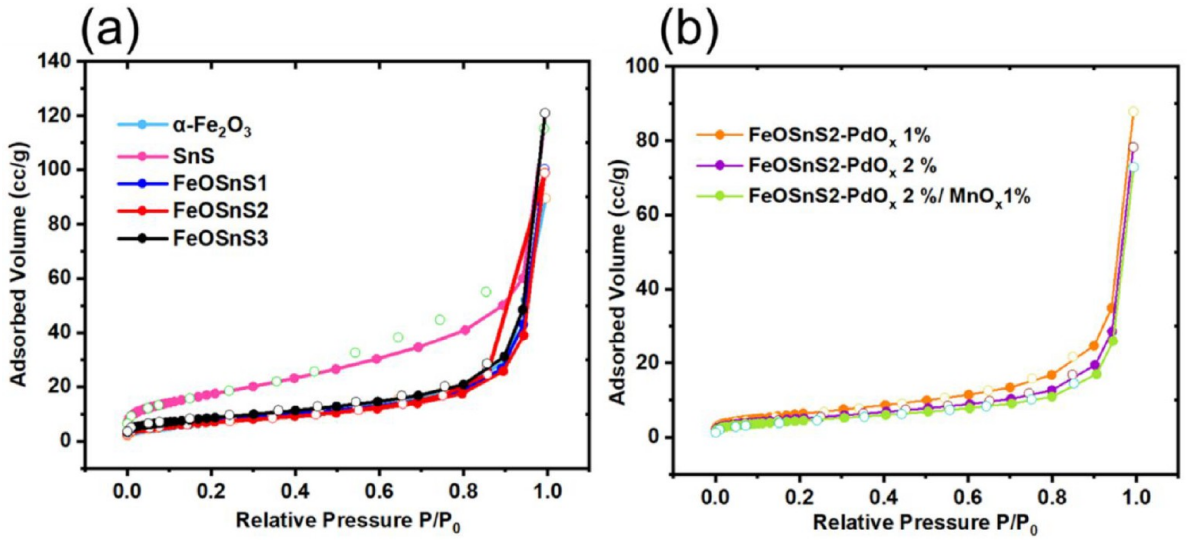

Figure 5. (a,b) N_2 adsorption−desorption isotherm of α-Fe_2O_3, SnS, FeOSnS1−3, and FeOSnS2-PdO_x/MnO_x catalysts measured at 77 K. Filled circles = adsorption points; empty circles = desorption points.

centered at 24 eV (Sn 4d), 486.4 eV (Sn $3d_{5/2}$), 494.9 eV (Sn $3d_{3/2}$), 713.6 eV (Sn $3p_{3/2}$), and 755.2 eV (Sn $3p_{1/2}$) (Figure 6(a)). The deconvolution of the Sn 3d energy state (Figure 6(e)) revealed spin−orbit doublet peaks at 486.4 eV (Sn $3d_{5/2}$) and 494.9 eV (Sn $3d_{3/2}$) with a separation of 8.5 eV which confirms the oxidation state of +2 and the formation of single-phase SnS. In addition, two small peaks at slightly higher BEs of 487.8 (Sn $3d_{5/2}$) and 496.2 eV (Sn $3d_{3/2}$) are assigned to Sn^{4+}, indicating the partial oxidation of the edges of SnS due to the unstable state of Sn^{2+} at the annealing temperature (500 °C).[54] Overall, XPS analysis indicates SnS as the major phase and SnS_2 as an impurity in the FeOSnS2/PdO_x/MnO_x catalyst. The high-resolution Fe 2p spectrum in Figure 6(f) exhibits the BEs of Fe $2p_{3/2}$ and Fe $2p_{1/2}$ at 710.9 and 724.5 eV with additional satellite peaks at 734.7 eV. Taken together, the data verify the valence state of Fe ions as +3 in α-Fe_2O_3. The result indicates that calcination at 500 °C does not change the valence state of Fe^{3+} to reduced or oxidized forms (e.g., Fe^{2+} or Fe^{4+}). Notably, as marked in the dotted square in the low-resolution survey spectrum (Figure 6(a)), the core-level lines assigned to Sn 3p located at BEs of 715.6 eV for Sn $3p_{3/2}$ and 757.7 eV for Sn $3p_{1/2}$ overlap with the Fe 2p core levels.[55] The core-level high-resolution orbital scan of the Pd 3d spectra were deconvoluted into four peaks centered at BEs of 336.9, 335.4, 342.4, and 343.5 eV, respectively (Figure 6(g)). The high intensity peaks at BEs of 336.9 ($3d_{5/2}$) and 342.4 eV ($3d_{3/2}$) are assigned to Pd^{2+} from the palladium precursor ($PdCl_2$) or PdO, which is in agreement with the reported value of the BE at 336.8−337.4 eV.[56] The very low intensity peaks at BEs of 337.7 and 343.5 eV are attributed to Pd^{4+}, suggesting that a low percentage of Pd^{2+} has been oxidized during the impregnation/calcination process.[57] There was no metallic Pd (Pd^0) detected on the surface of the catalyst with typical BEs of 335.1 and 341.1 eV.[58] The high-resolution spectrum of Mn 2p exhibited two main peaks at BEs of 641.8 and 653.3 eV assigned to Mn $2p_{3/2}$ and Mn $2p_{1/2}$, respectively. The spin−orbit splitting energy value of Mn 2p was 11.5 eV, close to 11.6 eV as reported by Yu et al.[59] The peaks were deconvoluted to identify the chemical valence of the MnO_x cocatalyst. As can be seen from Figure 6(h), the Mn $2p_{1/2}$ and Mn $2p_{3/2}$ peaks can be resolved into two pairs of triplet peaks, respectively. The Mn $2p_{3/2}$ peaks at BEs of 640.6, 641.8, and 642.4 eV correspond to Mn^{2+} (MnO), Mn^{3+} (Mn_2O_3), and Mn^{4+} cations (MnO_2), respectively. Similarly, the Mn $2p_{1/2}$ peaks appeared at BEs of 652.4, 653.3, and 653.8 eV which correspond to Mn^{2+}, Mn^{3+}, and Mn^{4+} cations, respectively. These results indicate the coexistence of MnO, Mn_2O_3, and MnO_2 species. The loaded manganese oxide is labeled as MnO_x ($1 < x < 2$).[60]

2.6. Photocatalytic Reforming of Ethanol. Our initial investigations of the photocatalytic performance of as-synthesized α-Fe_2O_3, SnS, and FeOSnS1−3 heterocatalysts focused on their ability to act as water-splitting catalysts. While FeOSnS2 was found to have the optimum photocatalytic activity, H_2 generation was low over all samples (Figure S7 in the Supporting Information). Therefore, our efforts turned to the photocatalytic reforming of ethanol using the cocatalysts. To explore the effect of the cocatalysts on the photocatalytic activity, single PdO_x and dual PdO_x/MnO_x cocatalysts were loaded on FeOSnS2, and studies of the photocatalytic reforming of ethanol in ethanol/water solutions compared to bare FeOSnS2 were performed. The results are shown in Figure 7 and Table 1. A blank test was carried out without photo-irradiation in the presence of both ethanol and photocatalyst (entry 1), resulting in negligible photocatalytic production rates. This confirms that this reaction does proceed photocatalytically with photoirradiation in the presence of the photocatalyst. The photocatalytic reforming of ethanol using ethanol/water solutions with single and dual cocatalysts loaded on FeOSnS2 resulted in the production of H_2, with only trace amounts of CH_4 produced which is consistent with the results presented in the literature for both single and dual cocatalyst systems.[61] Product selectivity of H_2 among other possible gases reached 99% (Table 1), with the formation of other oxygenated organic compounds unable to be detected; therefore, this method produces very high levels of pure H_2 gas.

Time course data for H_2 formation in the photocatalytic reforming of ethanol over the FeOSnS2 and FeOSnS2/PdO_x/MnO_x catalysts are shown in Figure 7(a). An overall increase in H_2 formation yield with time of illumination was observed for all samples, but a low amount of H_2 (42 μmol/g) was produced from the noncatalyzed irradiation of ethanol after 3.5 h of illumination (Table 1). The FeOSnS2 sample produced a high amount of H_2 (702 μmol/g) after 3.5 h of illumination,

https://doi.org/10.1021/acsomega.2c05410
ACS Omega 2022, 7, 42347−42358

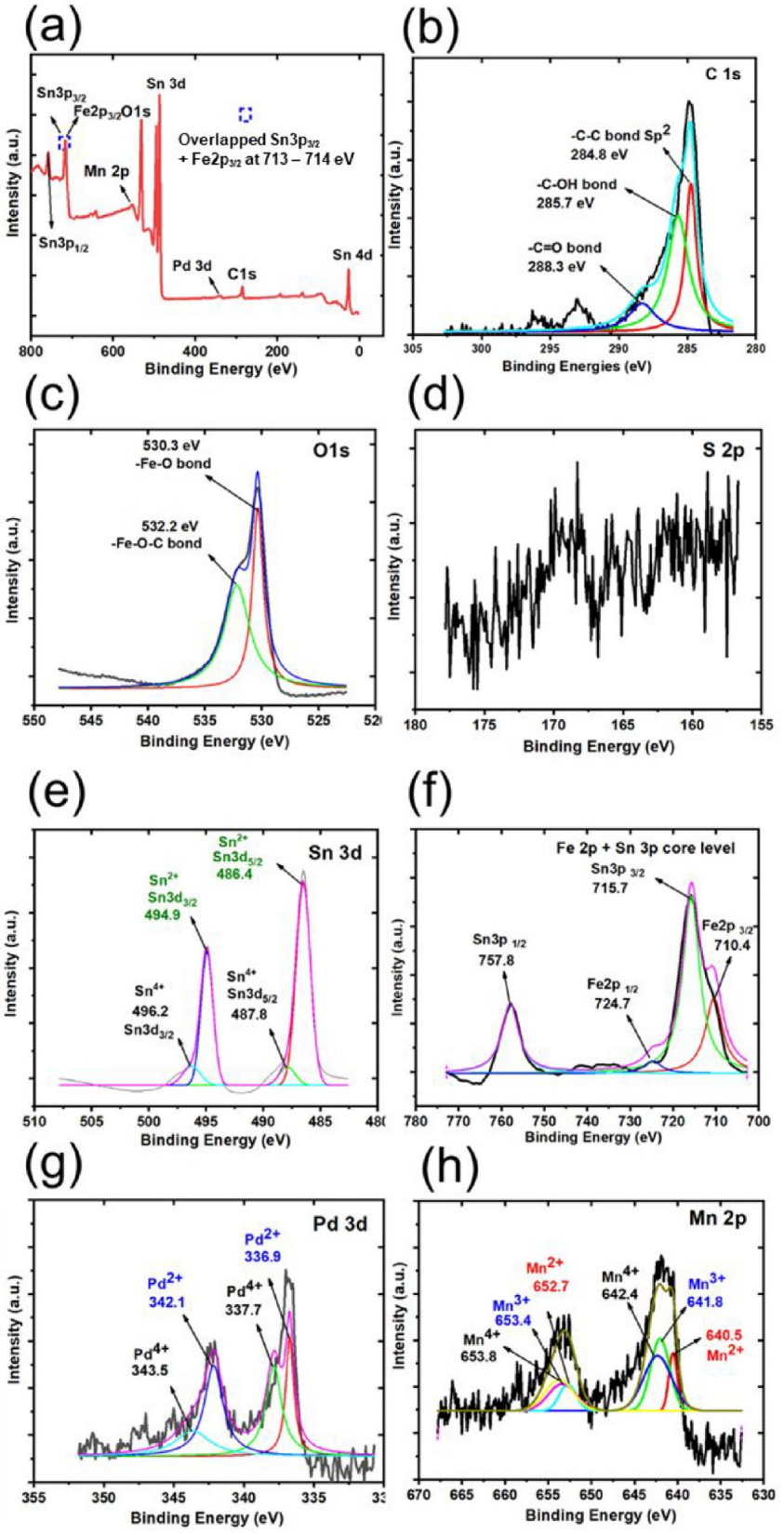

Figure 6. (a) XPS survey spectra and high-resolution XPS spectra of (b) C 1s, (c) O 1s, (d) S 2p, (e) Sn 3d, (f) Fe 2p, (g) Pd 3d, and (h) Mn 2p for FeOSnS2-PdO_x 2%/MnO_x 1% catalyst.

indicating the successful trapping of h^+ by ethanol during the reaction (Figure 7b).[62] The consumption of the photogenerated holes by ethanol results in the accumulation of photogenerated electrons on the photocatalyst surface, leading to a higher H_2 formation.[34] Our prepared FeOSnS2 heterocatalyst presents better performance than previously reported photocatalysts

https://doi.org/10.1021/acsomega.2c05410
ACS Omega 2022, 7, 42347−42358

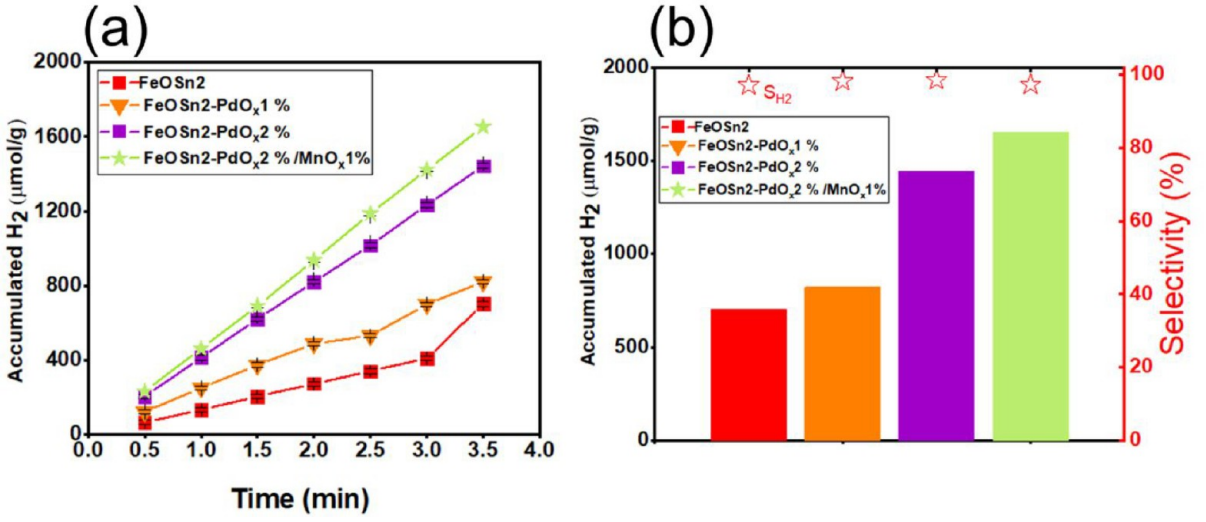

Figure 7. (a) Time course and (b) accumulated H_2 evolution amount from ethanol photoreforming over 1 g of FeOSnS2-PdO_x/MnO_x catalysts after a 3.5 h illumination (source: mercury lamp (4.4 mW cm^{-2} measured at λ = 254 ± 10 nm)).

Table 1. Product Yields for the Photocatalytic Reforming by Photocatalysts

			Production rate (μmol/g)				
Entry	Gas	Photocatalyst	H_2	CH_4	CO	CO_2	S_{H2}
	Ar	No light	-	-	-	-	-
1	Ar	FeOSnS2	702	1.75	-		99.75
2	Ar	FeOSnS2-PdO_x 1%	821	4.75	-	-	99.42
3	Ar	FeOSnS2-PdO_x 2%	1444	5.5	-	-	99.62
4	Ar	FeOSnS2-PdO_x 2%/MnO_x 1%	1654	11	-	-	99.33

consisting of α-Fe_2O_3 modified with other metal sulfides. For example, Lu et al. reported an HE rate of 6.9 μmol/g/h over Zn-doped α-Fe_2O_3-modified WS_2 after 2 h solar light irradiation.[63] Kadam et al. reported the highest HE rate of 136 μmol/g/h for a 10% Mo-doped SnS photocatalyst at 400 nm.[64] When PdO_x species were loaded as cocatalysts on FeOSnS2, H_2 formation yield was increased from 702 μmol/g for FeOSnS2 to 821 μmol/g for FeOSnS2-PdO_x 1% and 1444 μmol/g for FeOSnS2-PdO_x 2% after 3.5 h of illumination. The high H_2 formation yield for FeOSnS2-PdO_x 2% with a higher loading amount of PdO_x demonstrates that the photogenerated electrons and holes could be efficiently separated once PdO_x was loaded on the surface of FeOSnS2 by the impregnation method. The loading of the MnO_x species as an additional cocatalyst on FeOSnS2-PdO_x 2% can increase the H_2 formation yield from 1444 μmol/g for FeOSnS2-PdO_x 2% to 1654 μmol/g for the FeOSnS2-PdO_x 2%/MnO_x 1% photocatalyst under the same conditions. The formation of PdO_x and MnO_x cocatalysts was evidenced by XPS and UV−vis DRS analysis, confirming the role of dual cocatalysts of PdO_x/MnO_x in photocatalytic reforming of ethanol, where the PdO_x serves as an electron trap (catalytic sites for H_2 reduction) and MnO_x serves as a hole trap (catalytic sites for oxidation reaction). This vicinal charge separation by dual cocatalysts of PdO_x/MnO_x can also lead to efficient

Scheme 1. Band Bending and Carrier Transport at the Surface or Interface for FeOSnS2/PdO_x/MnO_x Catalysts

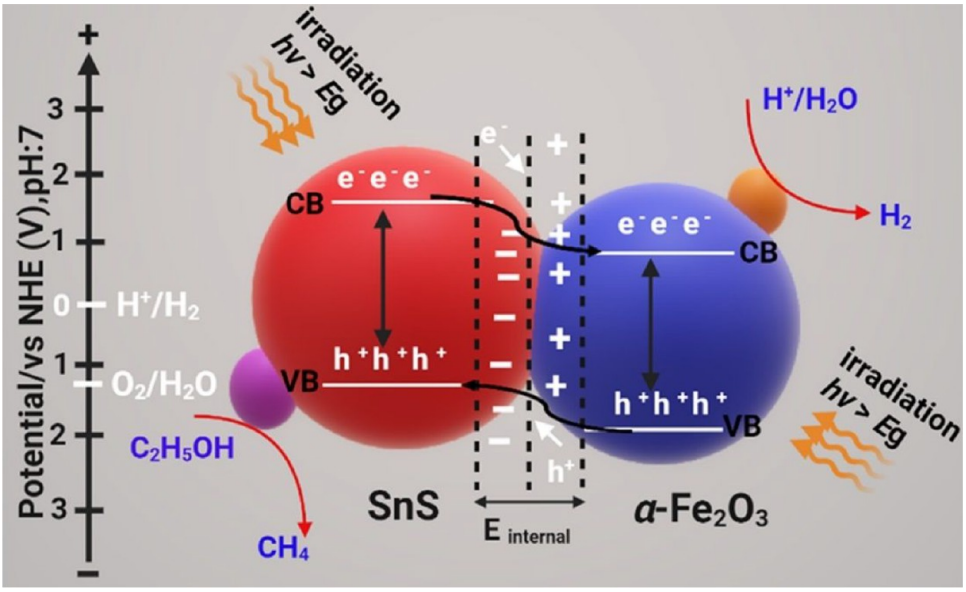

https://doi.org/10.1021/acsomega.2c05410
ACS Omega 2022, 7, 42347−42358

photocatalytic reforming of ethanol. Since reduction and oxidation reactions take place in a pair, any improvements in the oxidation would result in improved reduction and subsequent higher H_2 formation rates.[65] This indicates that the coexistence of reductive and oxidative cocatalysts could synergistically improve the photocatalytic potential. López-Martinez et al. observed the same phenomenon where the maximum HE rate of 728 μmol/m^2 was achieved over dual AuPd cocatalysts loaded onto SnS after 3 h irradiation (Xe lamp of 450 W and 100 mW/cm^2).[66]

2.7. Proposed Mechanism for H_2 Production. The possible charge separation at the interface of the PdO_x/MnO_x dual cocatalyst loaded on FeOSnS2 for the photocatalytic reforming of ethanol is depicted in Scheme 1. Before contact, the conduction band and valence band edge positions (E_{VB} and E_{CB}) of SnS and α-Fe_2O_3 catalysts are independent of each other and were calculated to be 2.89 and 0.96 eV for α-Fe_2O_3 and 1.04 and −0.40 eV for SnS (Supporting Information). The coupling of p-type SnS and n-type Fe_2O_3 forms a p−n junction at the heterostructure interfaces, which leads to the formation of an internal electric field ($E_{internal}$) between the p-type side and the n-type side and band bending.[67] At the p−n junction the electrons and holes are separated, and enhancement of the photogenerated electrons transferring from the CB of p-type SnS to the CB of n-type α-Fe_2O_3 (Scheme 1) occurs. Loading PdO_x and MnO_x on the FeOSnS2 surface improves the interface reaction speed because the cocatalysts can reduce the activation energy of the reduction and oxidation reaction for the photocatalytic reforming of ethanol. The TEM images revealed the PdO_x NPs were deposited on the surface of α-Fe_2O_3 and SnS. However, we could not determine the exact position of MnO_x on the surface of FeOSnS2, and it seems that MnO_x is randomly distributed on the surface of the FeOSnS2 catalyst. Considering the improved HE rate for the dual cocatalyst, one possible explanation may be that the loaded cocatalysts are sufficiently spatially separated that the recombination of electron/hole pairs is minimized. Therefore, PdO_x functions as the reduction site and receives the photoexcited electrons from the CB of α-Fe_2O_3 to produce H_2, while MnO_x functions as the oxidation site and receives the photoexcited holes from the CB of SnS to produce CH_4.

3. CONCLUSION

We have successfully synthesized FeOSnS heterocatalysts using a simple *in situ* chemical precipitation method. The prepared FeOSnS2 heterocatalyst exhibits excellent HE performance relative to pristine α-Fe_2O_3 and SnS, due to the new heterostructural interface provided by this technique. Loading of redox PdO_x and MnO_x cocatalysts did not influence the crystal structure of the FeOSnS2 heterocatalyst, but they were partially oxidized during loading. The loaded cocatalysts masked the pores of the FeOSnS2 heterocatalyst, resulting in the reduction of the active surface area (S_{BET}). HE results revealed the success of the undertaken strategies, namely, the integration of α-Fe_2O_3 and SnS and coloading of redox PdO_x and MnO_x cocatalysts. The highest HE rate was achieved for FeOSnS2-PdO_x 2%/MnO_x 1%, ascribed to the synergistic redox contribution of the PdO_x and MnO_x species. In order to increase the HE rate further, two strategies will be considered in future work including (i) the loading of cocatalysts using different methods onto the optimal heterocatalyst and (ii) altering the ratios of the loaded PdO_x and MnO_x cocatalysts.

4. EXPERIMENTAL SECTION

4.1. Materials. Iron(III) acetylacetonate ($Fe(acac)_3 \geq$ 99.9% trace metals basis), poly(vinylpyrrolidone) (PVP, average molecular weight 40,000 g mol^{-1}), *N*,*N*-dimethylformamide (DMF), sulfur powder (99.99%), and tin chloride dihydrate ($SnCl_2{\cdot}2H_2O$, 99%), were purchased from Sigma-Aldrich. All other chemicals were of analytical grade and used as received from commercial sources without further purification.

4.2. Synthesis of the α-Fe_2O_3 Catalyst. The α-Fe_2O_3 catalyst was synthesized through our previously published hydrothermal route.[68]

4.3. Synthesis of the SnS Catalyst. The flower-like SnS catalyst was synthesized by the above hydrothermal method, except $SnCl_2$ (0.2 mmol), PVP (0.4 mmol), and sulfur powder (0.1 mmol) precursors were mixed in DMF (20 mL) under stirring (500 rpm) at 70 °C for 120 min followed by hydrothermal reaction at 180 °C for 6 h and an eventual washing process as above.

4.4. Synthesis of α-Fe_2O_3−SnS (FeOSnS) Heterocatalysts. The *in situ* chemical precipitation method was utilized to synthesize FeOSnS heterocatalysts using different mass ratios of as-prepared SnS and α-Fe_2O_3 constituents to find the optimal formulation for coating with cocatalysats in the next step. In a typical experiment, SnS:α-Fe_2O_3 (1:1 w/w) was dispersed by ultrasonication in 50 mL of EtOH/H_2O solution (20:80 v/v) for 30 min and stirred in a fume hood at 80 °C for 24 h. The resultant product was collected by centrifugation, rinsed with distilled water and absolute ethanol three times, and dried at 80 °C for 6 h in an electric oven. The obtained heterocatalyst was denoted as FeOSnS1. Similarly, FeOSnS2 (SnS:α-Fe_2O_3 = 1.5:0.5 w/w) and FeOSnS3 (SnS:α-Fe_2O_3 = 0.5:1.5 w/w) were also prepared following the above procedure. The prepared FeOSnS1−3 heterocatalysts were then placed inside ceramic crucibles and calcined under Ar(g) at 500 °C for 5 h.

4.5. Loading of PdO_x/MnO_x Cocatalysts onto FeOSnS2. An impregnation method was utilized to load cocatalysts on the FeOSnS heterocatalyst. To synthesize FeOSnS2-PdO_x 1%, 0.5 g of FeOSnS2 was soaked in a solution (100 mL) containing the Pd precursor (0.008 g $PdCl_2$) and continuously stirred in a water bath at 120 rpm at 80 °C until the evaporation of the water from the suspension. The resulting solid was washed with absolute ethanol and distilled water three times and dried at 70 °C in an electric oven overnight followed by a calcination on a ceramic crucible in air at 350 °C for 2 h. FeOSnS2-PdO_x 2% and FeOSnS2-PdO_x 2%/MnO_x 1% catalysts were prepared using the same procedure with stoichiometric amounts of Pd (0.016 g of $PdCl_2$) and MnO_x precursors (0.016 g of $PdCl_2$ and 0.027 g of $Mn(NO_3)_2{\cdot}4H_2O$).

4.6. Ethanol Reforming for Hydrogen Production. The photocatalytic H_2 production was commenced by irradiation of the solution using a 100 W high-pressure mercury lamp (4.4 mW cm^{-2} measured at λ = 254 ± 10 nm). The amount of H_2 in the outlet gas was quantified by an online gas chromatograph (Shimadzu, GC-8A, TCD, Shincarbon ST column, argon carrier). The experiment was carried out using a 20:80 ethanol−water solution where ethanol was used as the sacrificial reagent to consume the photogenerated holes during the reaction. The selectivity toward H_2 evolution compared with CH_4, S_{H2}, was calculated using the formula:

$$S_{H2}\ (\%) = R_{H2}/(R_{H2} + R_{CH4}) \times 100$$

https://doi.org/10.1021/acsomega.2c05410
ACS Omega 2022, 7, 42347−42358

where R_{H2} and R_{CH4} describe the production rate of H_2 and CH_4, respectively. The amount of CO and CO_2 produced was negligible and not considered in this equation.

5. CHARACTERIZATION

Powder X-ray diffraction (PXRD) patterns were recorded on a Rigaku Spider X-ray diffractometer with Cu K_α radiation (λ = 1.5406 Å), at 40 kV and 50 mA from 10° to 80° in the Bragg configuration. The morphology of the catalysts was examined using transmission electron microscopy (TEM, Tecnai G2 Spirit Bio-TWIN, acceleration voltage of 200 Kv) and scanning electron microscopy (SEM, FE-SEM FEI Quanta 200). ImageJ software was acquired for postprocessing and particle size analysis. The elemental mapping images and energy-dispersive X-ray spectroscopy (EDX) spectra of catalysts were probed by an energy-dispersive spectrometer connected to field-emission scanning electron microscopy (FE-SEM FEI Quanta 200) to verify the chemical composition. The spectral data were collected with a silicon EDAX unit (NJ, USA) running Genesis Spectrum software (version 5.21). The EDS spectra were generated for each catalyst by a line scan of several randomly selected areas under different magnifications.

The chemical state of catalysts was probed with X-ray photoelectron spectroscopy (XPS) (Kratos Axis Ultra^{DLD} X-ray Photoelectron Spectrometer) at the pressure of 10^{-9} Torr with Al K_α X-rays (1486.69 eV) as the X-ray source. All spectra were calibrated with respect to the C 1s signal from adventitious hydrocarbon set at 285 eV. The high-resolution narrow-scan XPS spectra included nonlinear (Shirley) background subtraction and peak deconvolution by using mixed Gaussian−Lorentzian functions.

The mass percentages of PdO_x and MnO_x cocatalysts were analyzed by atomic absorption spectroscopy (AAS; GBC Scientific PerkinElmer Instrument) with a slit width of 0.2 nm, a lamp current of 5 mA, and an air-acetylene flame, with a Pd hollow cathode lamp (340.5 nm) and Mn hollow cathode lamp (403.1 nm) for PdO_x and MnO_x, respectively. For AAS analysis, approximately 5 mg of catalyst was digested in a mixture of concentrated HCl (37%, 0.5 mL), HNO_3 (70%, 1.0 mL), and H_2O_2 (32%, 1.0 mL) at 100 °C overnight followed by dilution to 50 mL with Milli-Q water. Standard 1000 ppm Pd in HCl and Mn in HNO_3 (Sigma-Aldrich) solutions were used to prepare metal calibration standard solutions (10−100 ppm) from which the intensity vs concentration plot was acquired for quantification.[69] The N_2 adsorption−desorption isotherms were analyzed on a Quantachrome BELSORP Mini Autosorb nitrogen-adsorption apparatus. Samples were evacuated at 120 °C for 20 h prior to Brunauer−Emmett−Teller (BET) measurements with autosorb at liquid nitrogen temperature (77 K). The BET specific surface area (S_{BET}) of the catalysts was investigated by a multipoint BET method utilizing the adsorption data in the relative pressure (P/P_0) range of 0−1.

The optical characteristics and band gap values of the catalysts were acquired via a UV−vis diffuse reflectance spectrometer (UV−vis DRS; V-640 (JASCO)) with an integrating sphere attachment in the wavelength range of 200−800 nm at RT. High-purity barium sulfate ($BaSO_4$) powder was used as a reflectance standard. Photoluminescence (PL) emission spectra were collected at RT using a Horiba Scientific Fluoromax-4 Spectrofluorometer. All samples with concentrations of 0.06 mg/mL in EtOH were excited at 330 nm with a 150 W ozone-free xenon arc lamp as the excitation source, and the emission spectra were recorded from 330 to 620 nm.

ASSOCIATED CONTENT

Supporting Information

The Supporting Information is available free of charge at https://pubs.acs.org/doi/10.1021/acsomega.2c05410.

TEM images and corresponding PdO_x particle size distribution for $FeOSnS_2$-PdO_x 2% and $FeOSnS_2$-PdO_x 2%/MnO_x 1%, ATR-FTIR results, table of physicochemical properties, UV−vis DRS and EDS spectra, table of wt % of the heterocatalysts, PL spectra, hysteresis loops, photocatalytic water splitting, and accompanying explanations (PDF)

AUTHOR INFORMATION

Corresponding Author

Paul G. Plieger − *School of Natural Sciences, Massey University, Palmerston North 4410, New Zealand;* orcid.org/0000-0003-4886-7677; Email: p.g.plieger@massey.ac.nz

Authors

Hossein Etemadi − *School of Natural Sciences, Massey University, Palmerston North 4410, New Zealand*

Tayyebeh Soltani − *Graduate School of Human and Environmental Studies, Kyoto University, Kyoto 606-8501, Japan*

Hisao Yoshida − *Graduate School of Human and Environmental Studies, Kyoto University, Kyoto 606-8501, Japan; Elements Strategy Initiative for Catalysts and Batteries (ESICB), Kyoto University, Kyoto 615-8520, Japan;* orcid.org/0000-0002-2540-0225

Yiming Zhang − *MacDiarmid Institute for Advanced Materials and Nanotechnology, School of Natural Sciences, Massey University, Palmerston North 4410, New Zealand*

Shane G. Telfer − *MacDiarmid Institute for Advanced Materials and Nanotechnology, School of Natural Sciences, Massey University, Palmerston North 4410, New Zealand;* orcid.org/0000-0003-1596-6652

Jenna K. Buchanan − *School of Natural Sciences, Massey University, Palmerston North 4410, New Zealand;* orcid.org/0000-0002-2501-5052

Complete contact information is available at: https://pubs.acs.org/10.1021/acsomega.2c05410

Author Contributions

H.E. designed and performed the synthetic experiments, collected characterization data, and wrote the draft manuscript. T.S. performed the H_2 production experiments and contributed to the writing of the H_2 production results. Y.Z. performed the BET and XRD measurements. S.G.T., H.Y., J.K.B., and P.G.P. provided an overall review of the manuscript. All authors read and approved the final manuscript.

Notes

The authors declare no competing financial interest.

ACKNOWLEDGMENTS

The authors gratefully acknowledge the New Zealand International Doctoral Research Scholarships (NZIDRS) committee for their financial support.

REFERENCES

(1) Puga, A. V.; Forneli, A.; García, H.; Corma, A. Production of H_2 by Ethanol Photoreforming on Au/TiO_2. *Adv. Funct. Mater.* **2014**, *24* (2), 241−248.

(2) Gombac, V.; Sordelli, L.; Montini, T.; Delgado, J. J.; Adamski, A.; Adami, G.; Cargnello, M.; Bernal, S.; Fornasiero, P. CuO_x-TiO_2 Photocatalysts for H_2 Production from Ethanol and Glycerol Solutions. *J. Phys. Chem. A* **2010**, *114* (11), 3916−3925.
(3) Hossain, A.; Sakthipandi, K.; Atique Ullah, A. K. M.; Roy, S. Recent Progress and Approaches on Carbon-Free Energy from Water Splitting. *Nano-Micro Lett.* **2019**, *11* (1), 103.
(4) Fujishima, A.; Honda, K. Electrochemical Photolysis of Water at a Semiconductor Electrode. *Nature* **1972**, *238* (5358), 37−38.
(5) Filice, S.; Fiorenza, R.; Reitano, R.; Scalese, S.; Sciré, S.; Fisicaro, G.; Deretzis, I.; La Magna, A.; Bongiorno, C.; Compagnini, G. TiO_2 Colloids Laser-Treated in Ethanol for Photocatalytic H_2 Production. *ACS Appl. Nano Mater.* **2020**, *3* (9), 9127−9140.
(6) Barreca, D.; Bigiani, L.; Monai, M.; Carraro, G.; Gasparotto, A.; Sada, C.; Martí-Sanchez, S.; Grau-Carbonell, A.; Arbiol, J.; Maccato, C.; Fornasiero, P. Supported Mn_3O_4 Nanosystems for Hydrogen Production through Ethanol Photoreforming. *Langmuir* **2018**, *34* (15), 4568−4574.
(7) Lee, K. M.; Lai, C. W.; Ngai, K. S.; Juan, J. C. Recent developments of zinc oxide based photocatalyst in water treatment technology: A review. *Water Res.* **2016**, *88*, 428−448.
(8) Zhu, Y.; Ling, Q.; Liu, Y.; Wang, H.; Zhu, Y. Photocatalytic performance of $BiPO_4$ nanorods adjusted via defects. *Appl. Catal., B* **2016**, *187*, 204−211.
(9) Meng, X.; Zhang, Z. Facile synthesis of $BiOBr/Bi_2WO_6$ heterojunction semiconductors with high visible-light-driven photocatalytic activity. *J. Photochem. Photobiol., A* **2015**, *310*, 33−44.
(10) Yourey, J. E.; Kurtz, J. B.; Bartlett, B. M. Water Oxidation on a $CuWO_4$-WO_3 Composite Electrode in the Presence of $[Fe(CN)_6]_3^-$: Toward Solar Z-Scheme Water Splitting at Zero Bias. *J. Phys. Chem. C* **2012**, *116* (4), 3200−3205.
(11) Wang, D.; Li, R.; Zhu, J.; Shi, J.; Han, J.; Zong, X.; Li, C. Photocatalytic Water Oxidation on $BiVO_4$ with the Electrocatalyst as an Oxidation Cocatalyst: Essential Relations between Electrocatalyst and Photocatalyst. *Phys. Chem. C* **2012**, *116* (8), 5082−5089.
(12) Bahnemann, D. W. Current challenges in photocatalysis: Improved photocatalysts and appropriate photoreactor engineering. *Res. Chem. Intermed.* **2000**, *26* (2), 207−220.
(13) Kollmannsberger, S. L.; Walenta, C. A.; Courtois, C.; Tschurl, M.; Heiz, U. Thermal Control of Selectivity in Photocatalytic, Water-Free Alcohol Photoreforming. *ACS Catal.* **2018**, *8* (12), 11076−11084.
(14) Mishra, M.; Chun, D.-M. α-Fe_2O_3 as a photocatalytic material: A review. *Appl. Catal. A-Gen.* **2015**, *498*, 126−141.
(15) Reddy, I. N.; Reddy, C. V.; Sreedhar, A.; Cho, M.; Kim, D.; Shim, J. Effect of plasmonic Ag nanowires on the photocatalytic activity of Cu doped Fe_2O_3 nanostructures photoanodes for superior photoelectrochemical water splitting applications. *J. Electroanal. Chem.* **2019**, *842*, 146−160.
(16) Jung, W.-S.; Park, S.-H.; Kadam, A. N.; Kim, H.; Lee, S.-W. Enhanced photoelectrochemical properties of α-Fe_2O_3. *Dalton Trans.* **2020**, *49* (9), 2924−2932.
(17) Wang, L.; Zhu, J.; Liu, X. Oxygen-Vacancy-Dominated Cocatalyst/Hematite Interface for Boosting Solar Water Splitting. *ACS Appl. Mater. Interfaces.* **2019**, *11* (25), 22272−22277.
(18) Zhu, S.; Yao, F.; Yin, C.; Li, Y.; Peng, W.; Ma, J.; Zhang, D. Fe_2O_3/TiO_2 photocatalyst of hierarchical structure for H_2 production from water under visible light irradiation. *Microporous Mesoporous Mater.* **2014**, *190*, 10−16.
(19) Shen, S.; Lindley, S. A.; Chen, X.; Zhang, J. Z. Hematite heterostructures for photoelectrochemical water splitting: rational materials design and charge carrier dynamics. *Energy Environ. Sci.* **2016**, *9* (9), 2744−2775.
(20) Bu, Q.; Li, S.; Wu, Q.; Bi, L.; Lin, Y.; Wang, D.; Zou, X.; Xie, T. Ferrihydrite-Modified Ti-Fe_2O_3 as an Effective Photoanode: The Role of Interface Interactions in Enhancing the Photocatalytic Activity of Water Oxidation. *ChemSusChem.* **2018**, *11* (19), 3486−3494.
(21) Ling, Y.; Wang, G.; Wang, H.; Yang, Y.; Li, Y. Low-Temperature Activation of Hematite Nanowires for Photoelectrochemical Water Oxidation. *ChemSusChem.* **2014**, *7* (3), 848−853.
(22) Li, F.; Li, J.; Zhang, J.; Gao, L.; Long, X.; Hu, Y.; Li, S.; Jin, J.; Ma, J. NiO Nanoparticles Anchored on Phosphorus-Doped α-Fe_2O_3 Nanoarrays: An Efficient Hole Extraction p-n Heterojunction Photoanode for Water Oxidation. *ChemSusChem.* **2018**, *11* (13), 2156−2164.
(23) Yi, S.-S.; Wulan, B.-R.; Yan, J.-M.; Jiang, Q. Highly Efficient Photoelectrochemical Water Splitting: Surface Modification of Cobalt-Phosphate-Loaded Co_3O_4/Fe_2O_3 p-n Heterojunction Nanorod Arrays. *Adv. Funct. Mater.* **2019**, *29* (11), 1801902.
(24) Carraro, G.; Maccato, C.; Gasparotto, A.; Montini, T.; Turner, S.; Lebedev, O. I.; Gombac, V.; Adami, G.; Van Tendeloo, G.; Barreca, D.; Fornasiero, P. Enhanced Hydrogen Production by Photoreforming of Renewable Oxygenates Through Nanostructured Fe_2O_3 Polymorphs. *Adv. Funct. Mater.* **2014**, *24* (3), 372−378.
(25) Wender, H.; Gonçalves, R. V.; Dias, C. S. B.; Zapata, M. J. M.; Zagonel, L. F.; Mendonça, E. C.; Teixeira, S. R.; Garcia, F. Photocatalytic hydrogen production of $Co(OH)_2$ nanoparticle-coated α-Fe_2O_3 nanorings. *Nanoscale.* **2013**, *5* (19), 9310−9316.
(26) Kim, J.; Kim, J.; Yoon, S.; Kang, J.-y.; Jeon, C.-W.; Jo, W. Single Phase Formation of SnS Competing with SnS_2 and Sn_2S_3 for Photovoltaic Applications: Optoelectronic Characteristics of Thin-Film Surfaces and Interfaces. *J. Phys. Chem. C* **2018**, *122* (6), 3523−3532.
(27) Mohan Kumar, G.; Fu, X.; Ilanchezhiyan, P.; Yuldashev, S. U.; Lee, D. J.; Cho, H. D.; Kang, T. W. Highly Sensitive Flexible Photodetectors Based on Self-Assembled Tin Monosulfide Nanoflakes with Graphene Electrodes. *ACS Appl. Mater. Interfaces* **2017**, *9* (37), 32142−32150.
(28) Ran, J.; Zhang, J.; Yu, J.; Jaroniec, M.; Qiao, S. Z. Earth-abundant cocatalysts for semiconductor-based photocatalytic water splitting. *Chem. Soc. Rev.* **2014**, *43* (22), 7787−7812.
(29) Lassoued, A.; Dkhil, B.; Gadri, A.; Ammar, S. Control of the shape and size of iron oxide (α-Fe_2O_3) nanoparticles synthesized through the chemical precipitation method. *Results Phys.* **2017**, *7*, 3007−3015.
(30) Rana, C.; Saha, S. Structural, optical and electrical characterization of SnS nanomaterials grown at different temperatures. *J. Mater. Sci.: Mater. Electron.* **2019**, *30* (24), 21160−21169.
(31) Yang, Z.; Chen, L.; Yang, Y.; Wang, J.; Huang, Y.; Liu, X.; Yang, S. Constructing TiO_2 decorated Bi_2WO_6 architectures with enhanced visible-light-driven photocatalytic activity. *Semicond. Sci. Technol.* **2017**, *32* (6), 065008.
(32) Zang, Y.; Li, L.; Li, X.; Lin, R.; Li, G. Synergistic collaboration of g-C_3N_4/SnO_2 composites for enhanced visible-light photocatalytic activity. *Chem. Eng. J.* **2014**, *246*, 277−286.
(33) Qi, K.; Li, Y.; Xie, Y.; Liu, S.-y.; Zheng, K.; Chen, Z.; Wang, R. Ag Loading Enhanced Photocatalytic Activity of g-C_3N_4 Porous Nanosheets for Decomposition of Organic Pollutants. *Front. Chem.* **2019**, DOI: 10.3389/fchem.2019.00091.
(34) Soltani, T.; Zhu, X.; Yamamoto, A.; Singh, S. P.; Fudo, E.; Tanaka, A.; Kominami, H.; Yoshida, H. Effect of transition metal oxide cocatalyst on the photocatalytic activity of Ag loaded $CaTiO_3$ for CO_2 reduction with water and water splitting. *Appl. Catal., B* **2021**, *286*, 119899.
(35) Jiang, Z.; Ding, D.; Wang, L.; Zhang, Y.; Zan, L. Interfacial effects of MnO x-loaded TiO 2 with exposed {001} facets and its catalytic activity for the photoreduction of CO 2. *Catal. Sci. Technol.* **2017**, *7* (14), 3065−3072.
(36) Mohamed, M. A.; Rahman, N. A.; Zain, M. F.; Minggu, L. J.; Kassim, M. B.; Jaafar, J.; Samad, S.; Mastuli, M. S.; Wong, R. J. Hematite microcube decorated TiO2 nanorods as heterojunction photocatalyst with in-situ carbon doping derived from polysaccharides bio-templates hydrothermal carbonization. *J. Alloys Compd.* **2020**, *820*, 153143.
(37) Imran, M.; Yousaf, A. B.; Kasak, P.; Zeb, A.; Zaidi, S. J. Highly efficient sustainable photocatalytic Z-scheme hydrogen production from an α-Fe_2O_3 engineered ZnCdS heterostructure. *J. Catal.* **2017**, *353*, 81−88.
(38) Li, S.; Jiang, W.; Xu, K.; Hu, S.; Liu, Y.; Zhou, Y.; Liu, J. Synthesis of Flower-Like AgI/BiOCOOH p-n Heterojunctions With Enhanced

Visible-Light Photocatalytic Performance for the Removal of Toxic Pollutants. *Front. Chem.* **2018**, DOI: 10.3389/fchem.2018.00518.
(39) Liang, S.; Zhou, Z.; Wu, X.; Zhu, S.; Bi, J.; Zhou, L.; Liu, M.; Wu, L. Constructing a MoS_2 QDs/CdS Core/Shell Flowerlike Nanosphere Hierarchical Heterostructure for the Enhanced Stability and Photocatalytic Activity. *Molecules (Basel, Switzerland)* **2016**, *21* (2), 213.
(40) Baby, B. H.; Bharathi Mohan, D. Phase optimization study of orthorhombic structured SnS nanorods from CTAB assisted polyol synthesis for higher efficiency thin film solar cells. *Sol. Energy.* **2018**, *174*, 373−385.
(41) Ding, D.; Rath, T.; Lanzetta, L.; Manuel Marin-Beloqui, J.; Haque, S. A. Efficient Hybrid Solar Cells Based on Solution Processed Mesoporous TiO_2/Tin(II) Sulfide Heterojunctions. *ACS Appl. Energy Mater.* **2018**, *1* (7), 3042−3047.
(42) Banu, S.; Ahn, S. J.; Eo, Y. J.; Gwak, J.; Cho, A. Tin monosulfide (SnS) thin films grown by liquid-phase deposition. *Sol. Energy.* **2017**, *145*, 33−41.
(43) Christoforidis, K. C.; Sengele, A.; Keller, V.; Keller, N. Single-Step Synthesis of SnS_2 Nanosheet-Decorated TiO_2 Anatase Nanofibers as Efficient Photocatalysts for the Degradation of Gas-Phase Diethylsulfide. *ACS Appl. Mater. Interfaces.* **2015**, *7* (34), 19324−19334.
(44) Liu, X.; Jin, A.; Jia, Y.; Jiang, J.; Hu, N.; Chen, X. Facile synthesis and enhanced visible-light photocatalytic activity of graphitic carbon nitride decorated with ultrafine Fe_2O_3 nanoparticles. *RSC Adv.* **2015**, *5* (112), 92033−92041.
(45) Shen, R.; Zhang, L.; Chen, X.; Jaroniec, M.; Li, N.; Li, X. Integrating 2D/2D CdS/α-Fe2O3 ultrathin bilayer Z-scheme heterojunction with metallic β-NiS nanosheet-based ohmic-junction for efficient photocatalytic H2 evolution. *Appl. Catal., B* **2020**, *266*, 118619.
(46) Si, H.-Y.; Mao, C.-J.; Xie, Y.-M.; Sun, X.-G.; Zhao, J.-J.; Zhou, N.; Wang, J.-Q.; Feng, W.-J.; Li, Y.-T. P-N depleted bulk BiOBr/α-Fe_2O_3 heterojunctions applied for unbiased solar water splitting. *Dalton Trans.* **2017**, *46* (1), 200−206.
(47) Yousatit, S.; Pitayachinchot, H.; Wijitrat, A.; Chaowamalee, S.; Nuntang, S.; Soontaranon, S.; Rugmai, S.; Yokoi, T.; Ngamcharussrivichai, C. Natural rubber as a renewable carbon source for mesoporous carbon/silica nanocomposites. *Sci. Rep.* **2020**, *10* (1), 12977.
(48) Zhu, Z.; Han, Y.; Chen, C.; Ding, Z.; Long, J.; Hou, Y. Reduced Graphene Oxide-Cadmium Sulfide Nanorods Decorated with Silver Nanoparticles for Efficient Photocatalytic Reduction Carbon Dioxide Under Visible Light. *ChemCatChem.* **2018**, *10* (7), 1627−1634.
(49) Huang, P.; Tao, W.; Wu, H.; Li, X.; Yin, T.; Zhang, Q.; Qi, W.; Gao, G.; Cui, D. N-doped coaxial CNTs@α-Fe_2O_3@C nanofibers as anode material for high performance lithium ion battery. *J. Energy Chem.* **2018**, *27* (5), 1453−1460.
(50) Thangavel, N.; Bellamkonda, S.; Arulraj, A. D.; Ranga Rao, G.; Neppolian, B. Visible light induced efficient hydrogen production through semiconductor-conductor-semiconductor (S-C-S) interfaces formed between g-C3N4 and rGO/Fe2O3 core-shell composites. *Catalysis Science & Technology* **2018**, *8* (19), 5081−5090.
(51) Shard, A. G. Detection limits in XPS for more than 6000 binary systems using Al and Mg Kα X-rays. *Surf. Interface Anal.* **2014**, *46* (3), 175−185.
(52) He, Z.; Wang, Y.; Dong, X.; Zheng, N.; Ma, H.; Zhang, X. Indium sulfide nanotubes with sulfur vacancies as an efficient photocatalyst for nitrogen fixation. *RSC Adv.* **2019**, *9* (38), 21646−21652.
(53) Kogo, G.; Xiao, B.; Danquah, S.; Lee, H.; Niyogushima, J.; Yarbrough, K.; Candadai, A.; Marconnet, A.; Pradhan, S. K.; Bahoura, M. A thin film efficient pn-junction thermoelectric device fabricated by self-align shadow mask. *Sci. Rep.* **2020**, *10* (1), 1067.
(54) Bandara, R. M. I.; Jayawardena, K. D. G. I.; Adeyemo, S. O.; Hinder, S. J.; Smith, J. A.; Thirimanne, H. M.; Wong, N. C.; Amin, F. M.; Freestone, B. G.; Parnell, A. J.; Lidzey, D. G.; Joyce, H. J.; Sporea, R. A.; Silva, S. R. P. Tin (IV) dopant removal through anti-solvent engineering enabling tin based perovskite solar cells with high charge carrier mobilities. *J. Mater. Chem. C* **2019**, *7* (27), 8389−8397.
(55) Leostean, C.; Pana, O.; Stefan, M.; Popa, A.; Toloman, D.; Senila, M.; Gutoiu, S.; Macavei, S. New properties of Fe_3O_4@SnO_2 core shell nanoparticles following interface charge/spin transfer. *Appl. Surf. Sci.* **2018**, *427*, 192−201.
(56) Xu, H.; Ni, K.; Li, X.; Fang, G.; Fan, G. Structural transformation of Pd-α-Fe_2O_3 and Pd-γ-Fe_2O_3 catalysts and application in the CO oxidation reaction. *RSC Adv.* **2017**, *7* (81), 51403−51410.
(57) Di, L.; Zhang, J.; Craven, M.; Wang, Y.; Wang, H.; Zhang, X.; Tu, X. Dehydrogenation of formic acid over Pd/C catalysts: insight into the cold plasma treatment. *Catal. Sci. Technol.* **2020**, *10* (18), 6129−6138.
(58) Kumar, A.; Srivastava, R. Pd-Decorated Magnetic Spinels for Selective Catalytic Reduction of Furfural: Interplay of a Framework-Substituted Transition Metal and Solvent in Selective Reduction. *ACS Appl. Energy Mater.* **2020**, *3* (10), 9928−9939.
(59) Meng, A.; Zhang, L.; Cheng, B.; Yu, J. TiO_2-MnO_x-Pt Hybrid Multiheterojunction Film Photocatalyst with Enhanced Photocatalytic CO_2-Reduction Activity. *ACS Appl. Mater. Interfaces.* **2019**, *11* (6), 5581−5589.
(60) Li, H.-b.; Huang, G.-y.; Zhang, J.; Fu, S.-h.; Wang, T.-g.; Liao, H.-w. Photochemical synthesis and enhanced photocatalytic activity of MnOx/$BiPO_4$ heterojunction. *Trans. Nonferrous Met. Soc. China.* **2017**, *27* (5), 1127−1133.
(61) Zhou, X.; Fang, Y.; Cai, X.; Zhang, S.; Yang, S.; Wang, H.; Zhong, X.; Fang, Y. In Situ Photodeposited Construction of Pt-CdS/g-C3N4-MnO x Composite Photocatalyst for Efficient Visible-Light-Driven Overall Water Splitting. *ACS Appl. Mater. Interfaces* **2020**, *12* (18), 20579−20588.
(62) Schneider, J. T.; Firak, D. S.; Ribeiro, R. R.; Peralta-Zamora, P. Use of scavenger agents in heterogeneous photocatalysis: truths, half-truths, and misinterpretations. *Phys. Chem. Chem. Phys.* **2020**, *22* (27), 15723−15733.
(63) Chu, D.; Li, K.; Liu, A.; Huang, J.; Zhang, C.; Yang, P.; Du, Y.; Lu, C. Zn-doped hematite modified by graphene-like WS_2: A p-type semiconductor hybrid photocathode for water splitting to produce hydrogen. *Int. J. Hydrog. Energy.* **2018**, *43* (15), 7307−7316.
(64) Kadam, S. R.; Ghosh, S.; Bar-Ziv, R.; Bar-Sadan, M. Structural Transformation of SnS_2 to SnS by Mo Doping Produces Electro/Photocatalyst for Hydrogen Production. *Chem. Eur. J.* **2020**, *26* (29), 6679−6685.
(65) Zhu, X.; Yamamoto, A.; Imai, S.; Tanaka, A.; Kominami, H.; Yoshida, H. A silver-manganese dual co-catalyst for selective reduction of carbon dioxide into carbon monoxide over a potassium hexatitanate photocatalyst with water. *Chem. Commun.* **2019**, *55* (90), 13514−13517.
(66) López-Martínez, S. D.; Juárez-Ramírez, I.; Torres-Martínez, L. M.; Babar, P.; Lokhande, A.; Kim, J. H. SnS-AuPd thin films for hydrogen production under solar light simulation. *J. Photochem. Photobiol., A* **2018**, *361*, 19−24.
(67) Soltani, T.; Lee, B.-K. Ag-doped $BiVO_4$/$BiFeO_3$ photoanode for highly efficient and stable photocatalytic and photoelectrochemical water splitting. *Sci. Total Environ.* **2020**, *736*, 138640.
(68) Etemadi, H.; Plieger, P. G. Improvements in the Organic-Phase Hydrothermal Synthesis of Monodisperse $M_xFe_{3-x}O_4$ (M = Fe, Mg, Zn) Spinel Nanoferrites for Magnetic Fluid Hyperthermia Application. *ACS Omega* **2020**, *5* (29), 18091−18104.
(69) Saha, S.; Martin, B.; Leonard, B.; Li, D. Probing synergetic effects between platinum nanoparticles deposited via atomic layer deposition and a molybdenum carbide nanotube support through surface characterization and device performance. *J. Mater. Chem. A* **2016**, *4* (23), 9253−9265.

https://doi.org/10.1021/acsomega.2c05410
ACS Omega 2022, 7, 42347−42358